Ocean Sci. Discuss., https://doi.org/10.5194/os-2018-4
Manuscript under review for journal Ocean Sci.
Discussion started: 28 February 2018

Electromagnetic characteristics of ENSO

Johannes Petereit [1,2], Jan Saynisch[1], Christopher Irrgang[1], Tobias Weber[1], and Maik Thomas[1,2]
[1]GFZ German Research Centre for Geosciences, Potsdam, Germany
[2]Freie Universität Berlin, Institute of Metereology, Berlin, Germany
Correspondence: Johannes Petereit (petereit@gfz-potsdam.de)

Abstract. The motion of electrically conducting sea water through Earth's magnetic field induces secondary electromagnetic fields. Due to its periodicity, the oceanic tidal-induced magnetic field is easily separable from magnetic field measurements and therefore detectable. These tidal-induced signatures in the electromagnetic fields are also sensitive to changes in oceanic temperature and salinity distributions. We investigate the impact of oceanic heat and salinity changes related to the El Niño/Southern Oscillation (ENSO) on oceanic tidal-induced magnetic fields. Hydrographic data containing characteristic ENSO dynamics have been derived from a coupled ocean-atmosphere simulation covering a period of 50 years. By applying a 3D induction model the corresponding tidal-induced magnetic signals have been calculated. By means of the Oceanic Niño Index (ONI), based on sea surface temperature anomalies, and the Magnetic Niño Index (MaNI), based on anomalies in the oceanic tidal-induced magnetic field, we demonstrate that evidence of developing ENSO events are found in the oceanic magnetic field statistically 4 months earlier than in sea surface temperatures. The analysis of the spatio-temporal progression of the oceanic magnetic field anomalies offers a deeper understanding on the underlying oceanic processes and is used to test and validate the initial findings.

1 Introduction

The El Niño/Southern Oscillation (ENSO) is well known for its warm and cold temperature anomalies caused by changes in the ocean-atmosphere system in the equatorial Pacific Ocean. These anomalous events, known as El Niño and La Niña, cause extreme weather conditions throughout the globe, e.g., tropical cyclones (Vincent et al., 2011), droughts, bush fires and floods (Philander, 1983). The extreme weather affects entire ecosystems (Glynn and De Weerdt, 1991) and causes damages to infrastructure and agricultural production (Wilhite et al., 1987). Substantial socio-economic costs are the consequence. The prospective doubling of extreme El Niño events, as a response to greenhouse warming (Cai et al., 2014), would increase the socio-economic costs even further. The negative impacts can be mitigated with pre-emptive measures provided reliable El Niño forecasts are available.

Knowledge about spatio-temporal variations of upper-ocean heat content are a major source of ENSO predictability (Meinen and McPhaden, 2000). Monitoring of seawater temperature and salinity anomalies are consequently a prerequisite for improved ENSO forecasting, especially since changes in thermocline depth, caused by equatorial Kelvin waves, have been known to precede sea surface temperature anomalies (Harrison and Schopf, 1984).

The measurement of these displacements with altimetric methods has been subject of extensive research (Ji et al., 2000; Picaut et al., 2002, 1996). A new and lesser known method to detect changes in the oceanic heat content are the motion-induced electromagnetic fields of the ocean (Minami, 2017; Saynisch et al., 2016). The flow of electrically conducting seawater generates an electric current caused by the interaction of moving salt ions with the geomagnetic field. The magnetic field induced by these electric currents can locally reach several nano Tesla (nT) (Maus and Kuvshinov, 2004).

The magnitudes of ocean flow and electric seawater conductivity determine the oceanic magnetic field strength in dependence of the field strength of the ambient geomagnetic field. The ocean flow generating seawater movements are classically divided into general ocean circulation and ocean tides.

The ocean circulation driven by wind and thermohaline circulation is irregular in time. Its effect are consequently difficult to separate from magnetic field measurements. However, the circulation-induced magnetic field's non-trivial contributions to the geomagnetic field have been subject of many studies (Tyler and Mysak, 1995; Manoj et al., 2006; Irrgang et al., 2016a, b). Manoj et al. (2006) analysed the influence of ENSO's changes in the equatorial current system on the circulation-induced magnetic field. They assumed a time-constant homogeneous conductivity distribution to derive the induced electrical current and found that the ENSO generated magnetic field anomalies were too small to be distinguishable from the magnetic field anomalies produced by the Antarctic circumpolar current with a magnitude of ± 0.2 nT.

The periodicity of the tidal flow on the other hand allows an easy separation of its magnetic field from other constituents in geomagnetic field measurements. Its signals have been extracted successfully for the semidiurnal M2 and N2 tides from measurements of the magnetic satellite missions CHAMP and Swarm (Tyler et al., 2003; Sabaka et al., 2016). Amplitude variations of these periodic magnetic signals are mainly caused by variations in seawater conductivity distribution. Seawater conductivity is sensitive to seawater temperature and salinity. These quantities exhibit high temporal variability in comparison to the amphidromic system of the tides. Consequently, the majority of information gained about anomalies of the oceanic tidally induced magnetic signals are linked to changes in oceanic temperature and salinity distributions. Modeled and measured tidal-induced magnetic fields are in good agreement (Tyler et al., 2003; Maus and Kuvshinov, 2004; Sabaka et al., 2016), offering the possibility for *in silico* sensitivity studies.

The influences of global climate variations, such as Greenland glacial melting and global warming, on the electromagnetic oceanic tidal-induced signals have already been investigated (Saynisch et al., 2016, 2017). For these cases, the tidal-induced radial magnetic field was found to be an appropriate measure to monitor climate variations of the global oceanic conductivity on decadal time scales.

With a period of 4-7 years, ENSO is acting on monthly to annual time scales. And despite its impact on the global climate, the immediate climatological influences on the ocean are limited to the region of the equatorial Pacific. ENSO's characteristic changes in the ocean circulation alter the pacific upper ocean temperature and salinity distributions ($\approx$ 300m) within months.

In our study, we follow the approach of Saynisch et al. (2017) and investigate whether the electromagnetic oceanic tidal-induced signals could be used as an appropriate measure for these changes in seawater conductivity and, consequently, the variating dynamics of the El Niño/Southern Oscillation.

Ocean Sci. Discuss., https://doi.org/10.5194/os-2018-4
Manuscript under review for journal Ocean Sci.
Discussion started: 28 February 2018

2 Models and Data

2.1 Ocean and tidal induced currents

We simulated ENSO with the ECHAM6/MPIOM a global coupled atmosphere-ocean model (Giorgetta et al., 2013).

The Max-Planck-Institute Ocean Model (MPIOM, (Jungclaus et al., 2013)) is a general ocean circulation model. The model solves the primitive equations for a hydrostatic Boussinesq fluid on a curvilinear Arakawa-C-grid with poles shifted to Antarctica and Greenland. The ocean is discretised on a grid with a horizontal resolution of $\sim 3.0° \times 1.8°$ (GR30) and an irregular vertical distribution over 40 horizontal levels.

The atmosphere general circulation model ECHAM6 (Stevens et al., 2013) is applied with the horizontal resolution of $\sim 3.75° \times 3.75°$ (T31) and 31 vertical hybrid sigma/pressure levels.

The simulated ocean data covers 50 years of monthly mean seawater temperature T, seawater salinity S and seawater pressure P. Using the Gibbs seawater equation (TEOS-10 (IOC et al., 2010)), the seawater conductivity σ can be calculated from, T, S and P. Present-day conditions were used to run the model in a free mode instead of a data-driven forcing. Therefore, the modeled climate represents reality only in a statistical sense.

The tidal-induced electric current, the source for the electromagnetic oceanic tidal signals (EMOTS), is derived for each month with the following two step algorithm.

First, the product of seawater conductivity σ and tidal velocities $\boldsymbol{v}_{\mathrm{M2}}$ is integrated from ocean bottom (-H) to surface (SSH)

$$\boldsymbol{V}_{\mathrm{M2}}(\varphi,\vartheta,t) = \int_{-H}^{SSH} \sigma(\varphi,\vartheta,z,t)\cdot \boldsymbol{v}_{\mathrm{M2}}(\varphi,\vartheta,z,t)\,dz, \tag{1}$$

where φ, ϑ and z are longitude, latitude and depth. The tidally induced electric current $\boldsymbol{j}_{\mathrm{M2}}$ is then calculated as the cross-product of the depth-integrated and conductivity-weighted transports $\boldsymbol{V}_{\mathrm{M2}}$ and the ambient geomagnetic field $\boldsymbol{B}_{\mathrm{Earth}}$ as

$$\boldsymbol{j}_{\mathrm{M2}}(\varphi,\vartheta) = \boldsymbol{V}_{\mathrm{M2}}(\varphi,\vartheta) \times \boldsymbol{B}_{\mathrm{Earth}}(\varphi,\vartheta). \tag{2}$$

Variations in the amphidromic system are negligible even on decadal time scales (Saynisch et al., 2016). Consequently, we followed the approach of Saynisch et al. (2017) and assumed the tidal system to be invariable in time. Tidal amplitudes and phases of the oceanic M2 tide were taken from the TPXO8-atlas (Egbert et al., 1994; Egbert and Erofeeva, 2002).

For this study, the geomagnetic field $\boldsymbol{B}_{\mathrm{Earth}}$ was estimated with the International Geomagnetic Reference Field edition IGRF-12 (Thébault et al., 2015). Our study focuses on the effects of oceanic conductivity variations. $\boldsymbol{B}_{\mathrm{Earth}}$ is consequently assumed to be constant in time. Naturally occurring secular variations in $\boldsymbol{B}_{\mathrm{Earth}}$ will linearly vary $\boldsymbol{j}_{\mathrm{M2}}$ (eq. (2)). Since the geomagnetic field is well know for real observation times (Gillet et al., 2010), the effects of its secular variations can easily be removed before analyzing observational data of EMOTS for the influence of ENSO.

2.2 EMOTS

The electromagnetic oceanic tidal signals are the electromagnetic response of interactions between the tidal electric current $\boldsymbol{j}_{\mathrm{M2}}$ and its electrically conducting environment. The EMOTS in our study are modeled with the induction model x3dg of Kuvshinov (2008). The model solutions are based on a volume integral approach combining the modified iterative dissipative method of Singer and Fainberg (1995) with a conjugate gradients iteration. For realistically modeled interactions, Earth's mantle conductivity and the oceanic conductivity need to be included in the model-setup (Grayver et al., 2016). The mantle conductivity is represented by a time constant 1-D spherical symmetric conductivity distribution following Püthe et al. (2015). The time variant ocean conductivity and the constant sediment conductance, depth-integrated conductivity, are represented by an inhomogeneous spherical conductance layer situated on top of the mantle conductivity. This conductance layer combines sediment conductance and modeled ocean conductance, derived from modeled T, S and P. The sediment conductance is a combined result of the method of Everett et al. (2003) with the global sediment thickness of Laske and Masters (1997).

2.3 Indices and statistical analysis

Different indices have been used to characterize ENSO events (Hanley et al., 2003). A current state-of-the-art indicator is the Oceanic Niño Index (ONI) (NOAA, 2017) from the climate prediction center of the National Oceanic and Atmospheric Administration (NOAA). The ONI is used to monitor the oceanic part of the ocean-atmosphere phenomenon. It is defined as a 3 months running mean of sea surface temperature anomalies in the Niño 3.4 region (i.e., 5°N - 5°S, 120°W - 170°W) relative to the mean annual signal of regularly updated 30-year base periods. Warm and cold events are identified as periods exceeding a threshold of ± 0.5°C longer than 4 months. The sea surface temperatures of the Niño 3.4 region have been known to correlate well with ENSO (Bamston et al., 1997).

In our study, the ONI calculations are based on the data of the model climate exeriment conducted with the ECHAM6/MPIOM. Since no significant trends are present in our data, we used all 50 years as a base period for the ONI calculation, instead of the running 30 year base period used by NOAA.

We also calculate a comparable index based on the radial tidal-induced magnetic field B_r (see section 2.2), the Magnetic Niño Index (MaNI). The same algorithm as in the ONI calculation is used with the difference that the sea surface temperature anomalies are substituted with B_r anomalies in the Niño 3.4 region.

The relation of the indices is analysed by calculating their correlation. A time delay analysis is carried out by calculating and analysing the cross-correlation. For two time series, the cross-correlation is the evolution of correlation between those two when they are shifted against each other in time. It is used to identify temporally lagging or leading signals.

3 Results and Discussion

3.1 Comparison of derived ENSO indices

From our modeled data, we derived two indices (see sec. 2.3). First, following the algorithm of the National Oceanic and Atmosphere Administration (NOAA), we calculated the classical Oceanic Niño Index (ONI) from seasurface temperatures (SST). Then, we adapted the algorithm for the modeled tidal-induced magnetic fields and created a Magnetic Niño Index (MaNI). The time series of both indices are shown in figure 1. In agreement with the NOAA classification (NOAA, 2017), 7 El Niños and 10 La Niñas can be found in the climate model data. Following Null (2017), 1 out of the 7 El Niños is classified as very strong ($\geq 2.0°$ C), 3 are found to be moderate (1.0 to $1.4°$ C) and 3 are classified as weak (0.5 to $0.9°$ C). The set of La Niña events consists of 6 moderate (-1.0 to $-1.4°$ C) and 4 weak events (-0.5 to $-0.9°$ C).

The strongest El Niño, the very strong warm event, is found at the most prominent peak of the time series. Starting at month 133 of the modeled time period, it lasts 16 months and reaches a maximum value of 2.3° C (figure 1). These values are comparable to that of the El Niño events taken place in winter 1997/8 or 2015/6, with anomalies of 2.3° C and durations of 13 and 19 months, respectively (NOAA, 2017).

The spatially averaged temporal mean radial oceanic magnetic field signal (B_r) in the Niño 3.4 region was found to be 0.546 nT with a mean seasonal variation of ± 0.29 pT (pikoTesla). The MaNI-range of -0.84 pT to 0.82 pT is in the same order of magnitude as the seasonal variation. Currently, high performance magnetic field sensors reach noise levels as low as 0.3 fT/$\sqrt{\text{Hz}}$ (Schmelz et al., 2011), while field magnetometers reach noise levels of 50 fT/$\sqrt{\text{Hz}}$. They consequently achieve, when measuring with an appropriate bandwith, a precision in the Femtotesla scale. Combined with the simple detectability of the periodic tidal part in magnetic field measurements, it is reasonable to assume that ENSO induced B_r anomalies will become detectable within years.

While the ONI covers the development of sea surface processes, the MaNI also includes subsurface processes. B_r is an integral measure incorporating the seawater conductivity integrated from ocean bottom to sea surface (see eq. (1) and eq. (2) in sec. 2). Despite their different perspectives on oceanic processes, both indices show a correlation of 0.63. The SST based index ONI is used to quantify the duration and strength of anomalous ENSO events. The high correlation of both indices shows that ENSO's effects have considerable impact on sea surface processes (ONI) as well as subsurface processes integrated in the tidal magnetic field.

The analysis of the cross-correlation of the two indices (embedded plot in figure 1) shows a MaNI-lead of 4 months over the ONI. Accounting for this lead, the correlation of both time series increases to 0.72.

Since in our setup (see sec. 2.2) the only time-variable contribution to B_r is the seawater conductivity σ, we conclude that in the Niño 3.4 region subsurface anomalies of σ, caused by anomalies in S and T, are leading SST anomalies.

Ocean Sci. Discuss., https://doi.org/10.5194/os-2018-4
Manuscript under review for journal Ocean Sci.
Discussion started: 28 February 2018

3.2 Spatio-temporal anomaly development

Temporal and spatial development of SST and B_r anomalies of the strongest ENSO cycle of the time series (grey shaded interval in figure 1) are displayed as Hovmoeller plots in figure 2. The findings for the other regular ENSO cycles are similar (not shown).

The geomagnetic equator and the spatial distribution of the tidal flow decrease the amplitude of B_r locally to 0 nT. These disturbing influences are diminished by spatially averaging SST and B_r anomalies from 5°S to 5°N. Vertical lines in figure 2b are remaining artefacts of the influences.

The comparison of figure 2a and figure 2b shows the lead of B_r anomalies over SST anomalies. Positive B_r anomalies emerge almost a year before they form in SST (phase I). The same is found for negative B_r anomalies. They emerge months before positive SST anomalies recede and mark the end of El Niño (phase III).

With the beginning of phase I, a positive B_r anomaly is found west of the Niño 3.4 region, while at sea surface cold or neutral conditions are found. Then positive B_r anomalies travel through the Niño 3.4 region eastwards. They are probably caused by equatorial Kelvin waves which are known to precede the onset of El Niño (Harrison and Schopf, 1984). Kelvin waves deepen the thermocline and increase the amount of warm seawater in the water column. A rise in seawater conductance, the depth-integrated seawater conductivity, is the consequence. SST anomalies have not yet formed during this phase. An intensification of positive B_r anomalies on the South American west coast is observed with the arrival of the Kelvin waves several months before the ONI-defined start of El Niño. This is explainable by the deepening of the thermocline (Wang and Picaut, 2013) and the corresponding anomalous increase of warm water in the upper ocean.

During phase II, El Niño effects become apparent at the sea surface. Here, the El Niño typical weakening of trade winds leads to changes of wind patterns in the Walker Circulation and alters the equatorial ocean current system (McPhaden, 1999). As a consquence, the warm water of the Western Warm Pool flows eastward and leads to an increase and westward expansion of SST anomalies at the Peruvian coast. The eastward migrating warm water causes a thermocline shallowing in the Western Warm Pool and a simultaneous deepening of the thermocline at the Peruvian coast. This leads to negative (positive) B_r anomalies west (east) of the Niño 3.4 region reaching local amplitudes of -6 pT (3 pT) when El Niño has fully developed. The general agreement of ONI and MaNI during this phase and the co-occurring maxima of both indices show that sea surface and subsurface dynamics exhibit a similar behaviour under the influence of a common cause.

The beginning of phase III is marked by an eastward expansion of the western negative B_r anomaly that has formed during phase II. The effects of El Niño, in form of warm SST anomalies, are still present for several months. Subsurface processes, however, cause an early decrease in B_r anomalies and consequently in MaNI. The eastern positive B_r anomaly recedes and a negative anomaly forms months before the onset of La Niña becomes apparent in ONI.

Phase IV marks the beginning of La Niña at sea surface. The Walker Circulation returns to normal conditions and the westward direction of the equatorial ocean current is re-established. Hence, the eastern thermocline shallows due to upwelling of cold water and warm surface water is transported to the western warm pool. Westward traveling SST and B_r anomalies are the consequence which increases the agreement of ONI and MaNI.

Ocean Sci. Discuss., https://doi.org/10.5194/os-2018-4
Manuscript under review for journal Ocean Sci.
Discussion started: 28 February 2018

With the end of phase IV a new cycle starts. The build-up of positive B_r anomalies, as described in Phase I, can be observed towards the end of the plotted time interval.

The analysis shows that the identified lead in the MaNI is not just a mere forward shift of the signals but a combined result of multiple effects. We found that it is a combination of early signs for the onset of the El Niño probably caused by eastward traveling Kelvin waves and a decrease in the magnetic signal months before the actual end of El Niño due to a shallowing of the thermocline. Consequently, the cycle of B_r anomalies and SST anomalies are phase-shifted.

3.3 Cross-correlation ONI and conductance

The findings obtained from calculating the cross-correlation between the oceanic conductance and the ONI at each grid point are summarized in figure 3.

In figure 3a, the maximum conductance anomaly of the time series at each grid point is shown. The magnitude of conductance anomalies is linked to the magnitude of relative B_r changes. The largest signals are therefore evident in the Western Warm Pool and at the west coast of South America. In these regions, the thermocline undergoes the largest relative changes as a result of ENSO. We also find that the conductance anomalies are elevated in a small band throughout the whole equatorial region. This region is the passage way of the equatorial Kelvin waves which vary the thermocline depth.

In figure 3b, the maximum absolute correlation is plotted. Largest values are found east of the Niño 3.4 region. The correlation the conductance and the ONI decreases westwards in a tongue shaped pattern, like the typical SST anomalies of El Niño and La Niña.

Figure 3c shows the lag between the ONI and the conductance. The lead in conductance increases in a tongue shaped pattern originating from the South American west coast. Since the Kelvin waves travel eastwards, an increase in the lead towards their origin is a logic consequence.

For the Niño 3.4 region (solid rectangles in figure 3), we find the same characteristics as for the analysis in section 3.1. The maximum absolute correlation of the whole region ranges from ≈ 0.7 to ≈ 0.8 (fig. 3b). The lead distribution in the area is not uniform. A large part of the western half is leading by 5 months and decreases eastward to 2 months. The area-averaged B_r anomalies of the MaNI therefore produce a signal that is leading statistically by 4 months with a correlation between 0.7 and 0.8.

3.4 Qualitative application of findings

The robustness of our findings is tested with a reanalysis of the correlation between ONI and MaNI using an updated averaging region for the MaNI. The new region is located at 5°N - 5°S, 150°W - 170°W. It keeps the poleward extend of ±5° to account for an adequate averaging in consideration of the presence of the geomagnetic equator. The eastern boundary is shifted westwards to increase the lead in magnetic field anomalies over SST anomalies (see figure 3c). The westward shift is constrained by the maximum correlation found in figure 3b. A recalculation of the MaNI within the updated region is shown in figure 4.

The reanalysis shows an overall decrease in correlation between the two time series. For a lag of 0 month, the correlation is decreased from 0.63 to 0.38. The maximum correlation is decreased from 0.72 to 0.58, while the lead is increased from 4 to 5 months. Additionally, the range of the updated MaNI has reduced from -0.84 pT to 0.82 pT to a range of -0.69 pT to 0.61 pT. These results are in agreement with the previous findings of section 3.3. We conclude that the lead in MaNI found in section 3.1 and 3.2 is caused by the lead in conductance anomalies found in section 3.3.

Correlation and cross-correlation are a linear measure for the relation between two variables. ENSO is the defining influence on the progression of ONI and MaNI. However, we found that the processes contributing to ENSO cause differing developments in sea surface and subsurface dynamics. Consequently, the decrease in correlation should be viewed as an increase in information gained from the perspectives of SST and B_r anomalies onto the same phenomenon.

4 Conclusions

Seawater temperature and salinity altering processes are known to be integrated in the electromagnetic oceanic tidal signals from bottom to surface. We investigated whether the tidal-induced magnetic fields could be used as an indicator for the El Niño/Southern Oscillation.

We used a coupled ocean-atmosphere general circulation model to simulate 50 years of monthly mean seawater temperature, salinity and pressure distributions. The properties were used to calculate the tidal electromagnetic signals for each month.

We analysed the relation of electromagnetic signals and ENSO by comparing two ENSO indices. These indices, calculated in the Niño 3.4 region, are the Oceanic Niño Index (ONI), based on SST anomalies, and the Magnetic Niño Index (MaNI), based on anomalies in the tidal magnetic field. Although, the modeled tidal magnetic field anomalies are too small to be detectable with contemporary measuring methods, we show that both indices are highly correlated and MaNI is leading the ONI by 4 months.

In order to explain this lead, the spatial and temporal evolution of B_r anomalies was analysed and compared with the evolution of SST anomalies. We found the lead to be explainable with eastward traveling equatorial Kelvin waves. They are known to precede the development of ENSO typical SST anomalies. They also increase the thermocline depth in the eastern Pacific ocean. In consequence, the electric conductance of the upper ocean is elevated which results in a stronger tidal magnetic field.

Based on these results, we analysed the relation between the ONI and equatorial Pacific conductance anomalies. The spatial distributions of correlation, lead and signal strength were in good agreement with the found MaNI characteristics. We showed that correlation of conductance anomalies and ONI increases eastward, while the lead over the ONI is increased westward.

With these findings we updated the averaging-region for the recalculation of the MaNI. With the new index, our interpretation was confirmed and the lead in MaNI was increased to 5 months. At the same time, signal strength and correlation were reduced. The decrease in correlation is interpreted as a gain in information about subsurface dynamics of ENSO rather than a loss in information about ENSO itself. Traditionally, researchers have focused on sea surface dynamics for signs of El Niño. The latest research, however, shows that subsurface dynamics play a crucial role in the build-up phase and the decline of El Niño. An increased focus on subsurface processes is therefore necessary to understand the El Niño/Southern Oscillation completely.

In summary, our study shows that the dynamic of tidally induced radial magnetic field anomalies contains information for an early awareness of developing anomalous warm and cold ENSO conditions. This, in return, may be used to improve current warning systems. Consequently, socio-economic effects brought into different regions of the Earth due to ENSO's teleconnections could be diminished with early pro-active counter measurements.

Author contributions. J.S. developed the concept for the study. T.W. performed the climate-experiment providing the necessary ENSO data. J.P., J.S. and C.I. designed all numerical experiments which where performed by J.P. The manuscript was written by J.P. with the assistance of J.S., C.I., T.W. and M.T. All authors discussed the results and commented on the manuscript.

Competing interests. The authors declare no competing financial interests.

Acknowledgements. This study is funded by the German Research Foundation's priority programme 1799 'Dynamic Earth' and by the Helmholtz Association of German Research Centres. We also want to thank the Max Planck Institute for Meteorology for making their climate model ECHAM6/MPIOM available to the research community. The model experiments were carried out an the supercomputing system of the German Climate Computation Centre (DKRZ) in Hamburg, Germany. We acknowledge the generation and distribution of the TPXO tidal data. Last but not least, we want to thank Alexey Kuvshinov for kindly providing his 3-D EM induction code and the model of the mantle conductivity. The work would not have been able without his training and help. Thank you.

References

Bamston, A. G., Chelliah, M., and Goldenberg, S. B.: Documentation of a highly ENSO related SST region in the equatorial Pacific: Research note, Atmosphere-Ocean, 35, 367–383, 1997.

Cai, W., Borlace, S., Lengaigne, M., Van Rensch, P., Collins, M., Vecchi, G., Timmermann, A., Santoso, A., McPhaden, M. J., Wu, L., et al.: Increasing frequency of extreme El Niño events due to greenhouse warming, Nature Climate Change, 4, 111–116, 2014.

Egbert, G. D. and Erofeeva, S. Y.: Efficient inverse modeling of barotropic ocean tides, Journal of Atmospheric and Oceanic Technology, 19, 183–204, 2002.

Egbert, G. D., Bennett, A. F., and Foreman, M. G.: TOPEX/POSEIDON tides estimated using a global inverse model, Journal of Geophysical Research: Oceans, 99, 24 821–24 852, 1994.

Everett, M. E., Constable, S., and Constable, C. G.: Effects of near-surface conductance on global satellite induction responses, Geophysical Journal International, 153, 277–286, 2003.

Gillet, N., Lesur, V., and Olsen, N.: Geomagnetic Core Field Secular Variation Models, Space Science Reviews, 155, 129–145, 2010.

Giorgetta, M. A., Jungclaus, J., Reick, C. H., Legutke, S., Bader, J., Böttinger, M., Brovkin, V., Crueger, T., Esch, M., Fieg, K., Glushak, K., Gayler, V., Haak, H., Hollweg, H.-D., Ilyina, T., Kinne, S., Kornblueh, L., Matei, D., Mauritsen, T., Mikolajewicz, U., Mueller, W., Notz, D., Pithan, F., Raddatz, T., Rast, S., Redler, R., Roeckner, E., Schmidt, H., Schnur, R., Segschneider, J., Six, K. D., Stockhause, M., Timmreck, C., Wegner, J., Widmann, H., Wieners, K.-H., Claussen, M., Marotzke, J., and Stevens, B.: Climate and carbon cycle changes from 1850 to 2100 in MPI-ESM simulations for the Coupled Model Intercomparison Project phase 5, Journal of Advances in Modeling Earth Systems, 5, 572–597, 2013.

Glynn, P. and De Weerdt, W.: Elimination of two reef-building hydrocorals following the 1982-83 El Nino warming event., Science(Washington), 253, 69–71, 1991.

Grayver, A. V., Schnepf, N. R., Kuvshinov, A. V., Sabaka, T. J., Manoj, C., and Olsen, N.: Satellite tidal magnetic signals constrain oceanic lithosphere-asthenosphere boundary, Science Advances, 2, 2016.

Hanley, D. E., Bourassa, M. A., O'Brien, J. J., Smith, S. R., and Spade, E. R.: A quantitative evaluation of ENSO indices, Journal of Climate, 16, 1249–1258, 2003.

Harrison, D. and Schopf, P. S.: Kelvin-wave-induced anomalous advection and the onset of surface warming in El Nino events, Monthly Weather Review, 112, 923–933, 1984.

IOC, SCOR, and APSO: The International thermodynamic equation of seawater–2010: Calculation and use of thermodynamic properties, Intergovernmental Oceanographic Commission, 2010.

Irrgang, C., Saynisch, J., and Thomas, M.: Impact of variable seawater conductivity on motional induction simulated with an ocean general circulation model, Ocean Sci., pp. 129–136, 2016a.

Irrgang, C., Saynisch, J., and Thomas, M.: Ensemble simulations of the magnetic field induced by global ocean circulation: Estimating the uncertainty, Journal of Geophysical Research: Oceans, 121, 1866–1880, 2016b.

Ji, M., Reynolds, R. W., and Behringer, D. W.: Use of TOPEX/Poseidon Sea Level Data for Ocean Analyses and ENSO Prediction: Some Early Results, Journal of Climate, 13, 216–231, 2000.

Jungclaus, J. H., Fischer, N., Haak, H., Lohmann, K., Marotzke, J., Matei, D., Mikolajewicz, U., Notz, D., and von Storch, J. S.: Characteristics of the ocean simulations in the Max Planck Institute Ocean Model (MPIOM) the ocean component of the MPI-Earth system model, Journal of Advances in Modeling Earth Systems, 5, 422–446, 2013.

Kuvshinov, A. V.: 3-D Global Induction in the Oceans and Solid Earth: Recent Progress in Modeling Magnetic and Electric Fields from Sources of Magnetospheric, Ionospheric and Oceanic Origin, Surveys in Geophysics, 29, 139–186, 2008.

Laske, G. and Masters, G.: A Global Digital Map of Sediment Thickness, EOS Trans. AGU, 78, 1997.

Manoj, C., Kuvshinov, A., Maus, S., and Lühr, H.: Ocean circulation generated magnetic signals, Earth, Planets and Space, 58, 429–437, 2006.

Maus, S. and Kuvshinov, A.: Ocean tidal signals in observatory and satellite magnetic measurements, Geophysical Research Letters, 31, 2004.

McPhaden, M. J.: Genesis and Evolution of the 1997-98 El Niño, Science, 283, 950–954, 1999.

Meinen, C. S. and McPhaden, M. J.: Observations of warm water volume changes in the equatorial Pacific and their relationship to El Niño and La Niña, Journal of Climate, 13, 3551–3559, 2000.

Minami, T.: Motional Induction by Tsunamis and Ocean Tides: 10 Years of Progress, Surveys in Geophysics, 2017.

NOAA: Cold & Warm Episodes by Season, http://www.cpc.ncep.noaa.gov/products/analysis_monitoring\/ensostuff/ensoyears2011.shtml, 2017.

Null, J.: El Niño and La Niña years and intensities, http://ggweather.com/enso/oni.htm, 2017.

Philander, S.: Meteorology: Anomalous El Niño of 1982–83, Nature, 305, 16–16, 1983.

Picaut, J., Ioualalen, M., Menkes, C., Delcroix, T., and McPhaden, M. J.: Mechanism of the Zonal Displacements of the Pacific Warm Pool: Implications for ENSO, Science, 274, 1486–1489, 1996.

Picaut, J., Hackert, E., Busalacchi, A. J., Murtugudde, R., and Lagerloef, G. S. E.: Mechanisms of the 1997-1998 El Niño-La Niña, as inferred from space-based observations, Journal of Geophysical Research: Oceans, 107, 5–1–5–18, 2002.

Püthe, C., Kuvshinov, A., Khan, A., and Olsen, N.: A new model of Earth's radial conductivity structure derived from over 10 yr of satellite and observatory magnetic data, Geophysical Journal International, 203, 1864, 2015.

Sabaka, T. J., Tyler, R. H., and Olsen, N.: Extracting ocean-generated tidal magnetic signals from Swarm data through satellite gradiometry, Geophysical Research Letters, 43, 3237–3245, 2016.

Saynisch, J., Petereit, J., Irrgang, C., Kuvshinov, A., and Thomas, M.: Impact of climate variability on the tidal oceanic magnetic signal - A model-based sensitivity study, Journal of Geophysical Research: Oceans, 121, 5931–5941, 2016.

Saynisch, J., Petereit, J., Irrgang, C., and Thomas, M.: Impact of oceanic warming on electromagnetic oceanic tidal signals: A CMIP5 climate model-based sensitivity study, Geophysical Research Letters, 44, 4994–5000, 2017.

Schmelz, M., Stolz, R., Zakosarenko, V., Schönau, T., Anders, S., Fritzsch, L., Mück, M., and Meyer, H.: Field-stable SQUID magnetometer with sub-fT Hz- 1/2 resolution based on sub-micrometer cross-type Josephson tunnel junctions, Superconductor Science and Technology, 24, 065 009, 2011.

Singer, B. S. and Fainberg, E.: Generalization of the iterative dissipative method for modeling electromagnetic fields in nonuniform media with displacement currents, Journal of applied geophysics, 34, 41–46, 1995.

Stevens, B., Giorgetta, M., Esch, M., Mauritsen, T., Crueger, T., Rast, S., Salzmann, M., Schmidt, H., Bader, J., Block, K., Brokopf, R., Fast, I., Kinne, S., Kornblueh, L., Lohmann, U., Pincus, R., Reichler, T., and Roeckner, E.: Atmospheric component of the MPI-M Earth System Model: ECHAM6, Journal of Advances in Modeling Earth Systems, 5, 146–172, 2013.

Thébault, E., Finlay, C. C., Beggan, C. D., Alken, P., Aubert, J., Barrois, O., Bertrand, F., Bondar, T., Boness, A., Brocco, L., Canet, E., Chambodut, A., Chulliat, A., Coïsson, P., Civet, F., Du, A., Fournier, A., Fratter, I., Gillet, N., Hamilton, B., Hamoudi, M., Hulot, G., Jager, T., Korte, M., Kuang, W., Lalanne, X., Langlais, B., Léger, J.-M., Lesur, V., Lowes, F. J., Macmillan, S., Mandea, M., Manoj,

Ocean Sci. Discuss., https://doi.org/10.5194/os-2018-4
Manuscript under review for journal Ocean Sci.
Discussion started: 28 February 2018

C., Maus, S., Olsen, N., Petrov, V., Ridley, V., Rother, M., Sabaka, T. J., Saturnino, D., Schachtschneider, R., Sirol, O., Tangborn, A., Thomson, A., Tøffner-Clausen, L., Vigneron, P., Wardinski, I., and Zvereva, T.: International Geomagnetic Reference Field: the 12th generation, Earth, Planets and Space, 67, 79, 2015.

Tyler, R. H. and Mysak, L. A.: Motionally-induced electromagnetic fields generated by idealized ocean currents, Geophysical & Astrophysical Fluid Dynamics, 80, 167–204, 1995.

Tyler, R. H., Maus, S., and Lühr, H.: Satellite Observations of Magnetic Fields Due to Ocean Tidal Flow, Science, 299, 239–241, 2003.

Vincent, E. M., Lengaigne, M., Menkes, C. E., Jourdain, N. C., Marchesiello, P., and Madec, G.: Interannual variability of the South Pacific Convergence Zone and implications for tropical cyclone genesis, Climate Dynamics, 36, 1881–1896, 2011.

Wang, C. and Picaut, J.: Understanding Enso Physics-A Review, pp. 21–48, American Geophysical Union, 2013.

Wilhite, D. A., Wood, D., and Meyer, S.: Climate-related impacts in the United States during the 1982-83 El Niño, 1987.

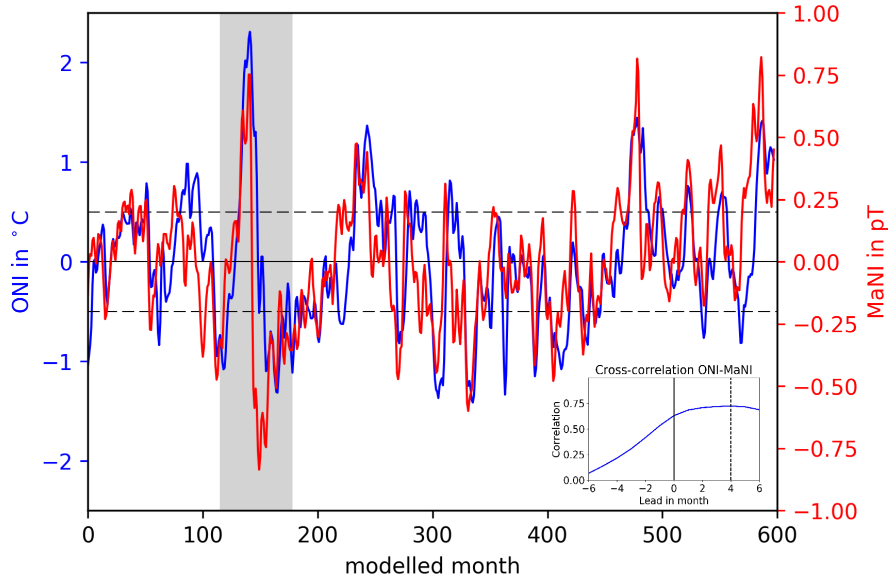

Figure 1. ENSO indices. ONI derived from sea surface temperatures (blue curve) and MaNI derived from the radial tidal induced magnetic field B_r (red curve). The dashed lines mark the threshold of ± 0.5 °C, the threshold for El Niño and La Niña events. The grey shaded area marks the strongest cycle of ENSO events (used for further analysis). The embedded plot shows the cross-correlation between ONI and MaNI. For positive leads, MaNI leads ONI.

Ocean Sci. Discuss., https://doi.org/10.5194/os-2018-4
Manuscript under review for journal Ocean Sci.
Discussion started: 28 February 2018

Ocean Science
Discussions

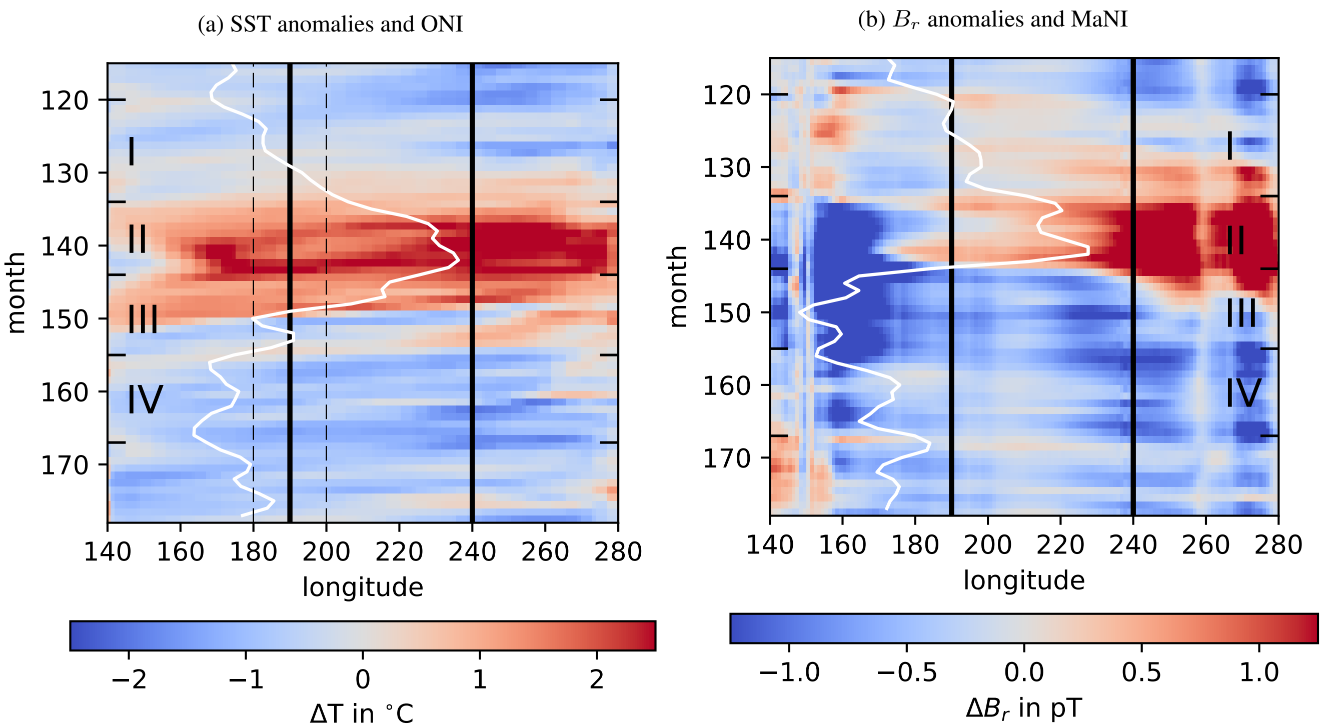

Figure 2. Hovmoeller plots of sea surface temperature anomalies (left) and B_r anomalies (right) averaged from 5°S to 5°N. The time interval shows the strongest ENSO cycle cf. figure 1. Vertical black lines enclose the Niño 3.4 region used to calculate ONI and MaNI. The solid white lines represent the indices derived from the individual anomalies centred on 170°E (20° of longitude correspond to 1° C (left) and 0.4 pT (right)). The dashed lines represent the ONI thresholds for El Niño/ La Niña of ± 5 $^\circ$C (left).

Ocean Sci. Discuss., https://doi.org/10.5194/os-2018-4
Manuscript under review for journal Ocean Sci.
Discussion started: 28 February 2018

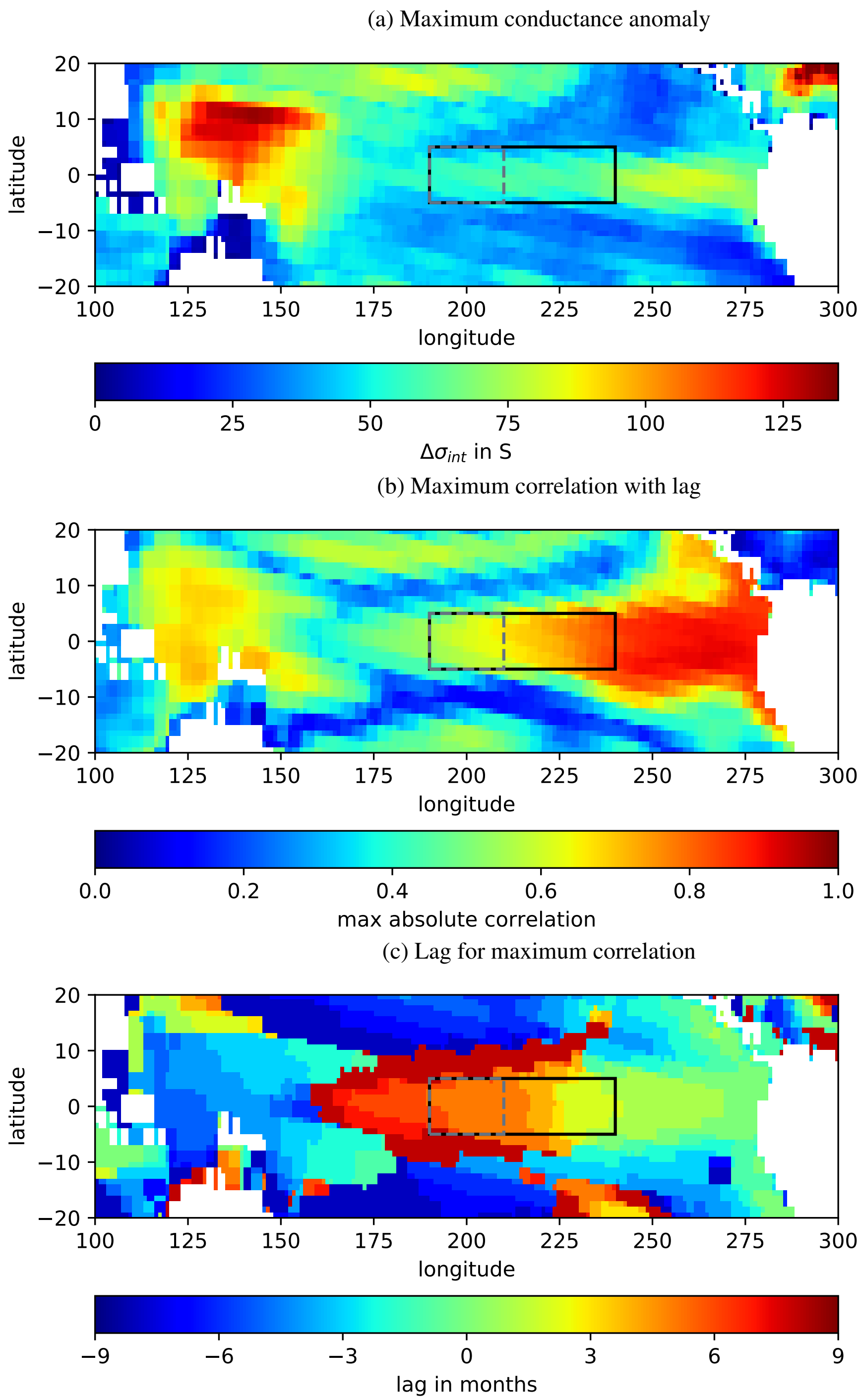

Figure 3. Cross-correlation analysis between the ONI and the conductance (σ_{int}) at each grid point: maximum absolute conductance anomaly (top), absolute maximum correlation, the peak value of the cross-correlation (middle), corresponding lead/lag to the absolute maximum correlation (bottom). The solid rectangle shows the location of the Niño 3.4 region, the dashed rectangle shows the location of an updated MaNI (5°N - 5°S, 150°W - 170°W).

Ocean Sci. Discuss., https://doi.org/10.5194/os-2018-4
Manuscript under review for journal Ocean Sci.
Discussion started: 28 February 2018

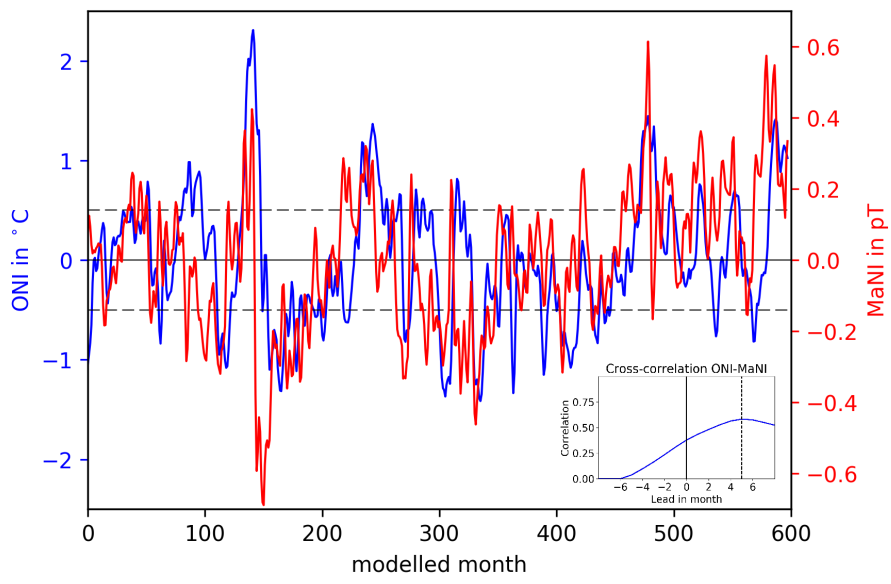

Figure 4. Comparison of time series of ONI (blue) and updated MaNI (red). Anomaly strength and correlation are reduced, while the lead is increased.